


Cite this: *Biomater. Sci.*, 2023, **11**, 828

# All-in-one CoFe<sub>2</sub>O<sub>4</sub>@Tf nanoagent with GSH depletion and tumor-targeted ability for mutually enhanced chemodynamic/photothermal synergistic therapy†

Niping Chen,<sup>a</sup> Yakun Wang,<sup>a</sup> Yaoxun Zeng,<sup>a</sup> Yushan Li,<sup>a</sup> Zhenxing Pan,<sup>a</sup> Haihong Li,<sup>a</sup> Jingman Chen,<sup>a</sup> Zefeng Chen,<sup>a</sup> Jiongpeng Yuan,<sup>a</sup> Wen Yan,<sup>c</sup> Yu-Jing Lu,<sup>a</sup> Xujie Liu,  \*<sup>a</sup> Yan He\*<sup>a</sup> and Kun Zhang<sup>a,b</sup>

In the complex and severe tumor microenvironment, the antitumor efficiency of nanomedicines is significantly limited by their low-efficacy monotherapy, non-tumor targeting, and systemic toxicity. Herein, to achieve tumor-targeted and enhanced chemodynamic/photothermal therapy (CDT/PTT), we fabricated an "all-in-one" biocompatible transferrin-loaded cobalt ferrate nanoparticle (CoFe<sub>2</sub>O<sub>4</sub>@Tf (CFOT)) with multiple functions by a simple solvothermal method and the following transferrin (Tf) functionalization. Upon exposure to 808 nm laser irradiation, CFOT, as a novel photothermal agent, exhibited outstanding phototherapeutic activity because of its excellent photothermal conversion efficiency ( $\eta = 46.5\%$ ) for high-performance PTT. Moreover, CFOT with multiple redox pairs could efficiently convert endogenous H<sub>2</sub>O<sub>2</sub> to hazardous hydroxyl radicals ( $\cdot\text{OH}$ ) via Fenton reactions while scavenging overexpressed GSH in the tumor microenvironment to realize self-reinforcing CDT. Importantly, CFOT undergoes a promoted Fenton-type reaction upon increasing the temperature under a photothermal effect and could augment PTT by high-level  $\cdot\text{OH}$ , exhibiting a considerably enhanced synergistic therapeutic effect. *In vitro* and *in vivo* experimental results demonstrated that CFOT has good potential as an "all-in-one" nanoagent to combine photothermal, chemodynamic, and tumor targeting for efficient tumor elimination.

Received 25th September 2022,

Accepted 18th November 2022

DOI: 10.1039/d2bm01542k

rsc.li/biomaterials-science

## 1. Introduction

Cancer still seriously threatens global health and life due to its high morbidity and mortality.<sup>1–3</sup> Under the defense of the complex tumor microenvironment, cancer cells possess supreme adaptability, robust drug resistance, aggressive multiplication, and metastasis, which makes it difficult to cure cancer efficiently and safely through conventional therapies due to their inherent drawbacks, such as multiple drug resistance (MDR), poor tumor-target specificity, and severe toxicity to normal cells.<sup>4–7</sup> With the development of nanomedicines, the emerging photothermal therapy (PTT) has been widely explored as a promising approach in cancer treatment on account of its

unique advantages, such as non-invasiveness, high efficacy, negligible tissue damage, and tumor specificity.<sup>8–11</sup> PTT usually employs photothermal agents (PTAs) to produce a local thermal effect at the tumor site under light irradiation, which could induce protein denaturation and nucleic acid degeneration to rapidly and irreversibly ablate tumor cells.<sup>12–15</sup> Nevertheless, the significant limitations of uneven heat distribution, the insufficient penetration depth of light, and overexpressed heat shock proteins allow some cancer cells to escape the destruction of thermal effects, causing tumor recurrence and disrupting PTT.<sup>16–18</sup> According to previous studies, excessive oxidation within tumor cells could enhance PTT by interfering with the tumor microenvironment and assisting therapy.<sup>19–22</sup> Therefore, combining polytherapy is desired to address the incompleteness of monotherapy for PTT.

In a reactive oxygen species (ROS)-mediated therapeutic modality, CDT generates large amounts of lethal hydroxyl radicals ( $\cdot\text{OH}$ ) via Fenton or Fenton-like reactions between hydrogen peroxide (H<sub>2</sub>O<sub>2</sub>) and metal ions (Co<sup>2+</sup>, Cu<sup>+</sup>, and Fe<sup>2+</sup>) for tumor treatment and synergistically enhanced PTT.<sup>23–25</sup> Given that the Fenton response occurs rapidly only under adequate H<sub>2</sub>O<sub>2</sub> and acidic conditions, CDT can be uniquely adapted to

<sup>a</sup>Allan H. Conney Laboratory for Anticancer Research, School of Biomedical and Pharmaceutical Sciences, Guangdong University of Technology, Guangzhou 510006, China. E-mail: liuxujie@gdut.edu.cn, heyan129@gdut.edu.cn

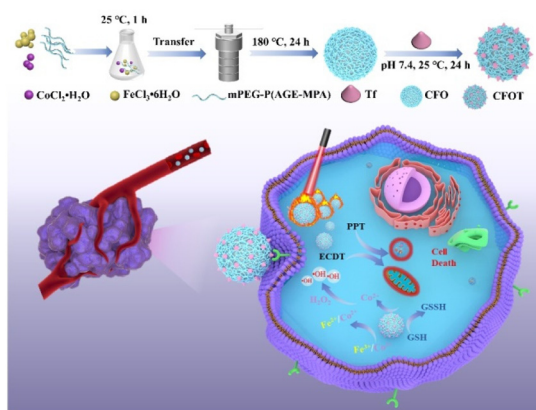
<sup>b</sup>School of Biotechnology and Health Sciences, Wuyi University, Jiangmen 529020, China

<sup>c</sup>Guangdong Second Provincial General Hospital, Guangzhou 510317, China

† Electronic supplementary information (ESI) available. See DOI: <https://doi.org/10.1039/d2bm01542k>

the tumor microenvironment (TME) to facilitate the precise and selective treatment of tumors while minimizing injury to normal tissue.<sup>26,27</sup> At the same time, Fenton-type reactions are accelerated at elevated temperatures and are independent of light stimulation; thus, CDT can continuously treat cancer cells that are not destroyed by light therapy for facilitating PTT to provide a “1 + 1 > 2” therapeutic effect and can help prevent tumor recurrence and distant metastasis.<sup>28–33</sup> However, glutathione (GSH) with high antioxidant capacity is overexpressed in tumor cells, which would significantly compromise the synergistic therapeutic effect. Therefore, regulating TME by depleting GSH could effectively improve tumor treatment.<sup>34–36</sup> For example, Wang *et al.* synthesized DOX@Cu<sup>2+</sup>/ZIF-8@PDA, which could consecutively deplete the overexpressed GSH and which showed excellent antitumor effects by synergistic PTT/CDT.<sup>37</sup> In addition, the specific targeting of tumors is a promising treatment method to improve the antitumor efficiency and biosafety of nanomedicines.<sup>38–40</sup> However, mainstream nanomedicines generally integrate multiple components through complex procedures to realize multitherapy, which drastically hinders their clinical application. Therefore, developing a multifunctional material with PTT/CDT synergy, GSH depletion, and tumor targeting through a simple process for safe and efficient antitumor therapy would be an extremely intelligent strategy.

Cobalt ferrite (CoFe<sub>2</sub>O<sub>4</sub>, abbreviated as CFO), a polycrystalline oxide, has been widely investigated in energy and environmental applications based on its multiple redox pairs (Co<sup>2+</sup>/Co<sup>3+</sup> and Fe<sup>2+</sup>/Fe<sup>3+</sup>) and high catalytic properties.<sup>41–44</sup> At the same time, CFO has a wide range of light absorption and can serve as a promising photothermal agent.<sup>45</sup> Qin's group reported CFO-BiOCl hierarchical microspheres, which had a photothermal enhancement effect through the modification of CoFe<sub>2</sub>O<sub>4</sub> under xenon lamp irradiation and achieved excellent organic pollutant degradation.<sup>46</sup> UV and visible light suffer from having a significant intensity and weak penetration, while near-infrared light (NIR) has biosafety and offers greater tissue penetration depth, and hence is more suitable for applications in the biological field.<sup>47</sup> Herein, an “all-in-one” nanoagent CoFe<sub>2</sub>O<sub>4</sub>@Tf (CFOT) was constructed by a simple solvothermal method and transferrin (Tf)-functionalized modification for enhanced-CDT/NIR-responsive PTT synergistic therapy along with an active targeting property (Scheme 1). On account of its significant photothermal conversion efficiency ( $\eta = 46.5\%$ ) under 808 nm laser irradiation, CFOT exhibited significant tumor-killing potential at high temperatures of PTT. Meanwhile, CFOT with multivalent metal ions was enabled with excellent ·OH generation performance and GSH consumption, and fulfilled self-enhanced CDT and assisted the PTT effect. This synergistic therapy with multiple enhanced CDT/PTT induced enhanced lipid peroxidation and further enhanced the damage to lysosomes and mitochondria to significantly kill tumor cells (HepG2, H22) and severely inhibited tumor growth. Furthermore, loading transferrin could increase the effective enrichment of CFOT in tumor cells, thus enhancing the synergistic antitumor effect and



**Scheme 1** Fabrication process of CFOT and schematic illustration mechanism of CFOT for PTT/CDT synergistic therapy with GSH depletion and tumor targeting.

reducing the damage to normal cells.<sup>48,49</sup> Hence, this work provides an efficient method for combining PTT and GSH depletion enhanced CDT on the same nanoplatform for high-efficiency selective targeting synergistic antitumor therapy.

## 2. Results and discussion

### 2.1. Synthesis and characterization

CFO was synthesized using a simple solvent-thermal method with poly (ethylene glycol)-poly (allyl glycidyl ether-3 mercaptopropionic acid) (mPEG-P(AGE-MPA)) as a stabilizer to enhance the hydrophilicity and biocompatibility.<sup>50</sup> The effective synthesis of mPEG-P(AGE-MPA) was demonstrated by the <sup>1</sup>H NMR spectra (Fig. S1†). Subsequently, the CFO was functionalized with transferrin to obtain CFOT, which was endowed with a tumor-targeting capability. The as-synthesized CFO and CFOT displayed irregular morphologies (Fig. 1a and b). High-resolution TEM (HRTEM) indicated that the lattice spacing of CFOT was 0.292 nm (Fig. S2a†), corresponding well with the (220) plane of CoFe<sub>2</sub>O<sub>4</sub>. The energy dispersive spectrometry (EDS) and elemental mapping analyses indicated the homogeneous distribution of Co, Fe, O, N, and S in CFOT (Fig. S3† and Fig. 1c), confirming the chemical composition of CFOT. The X-ray diffraction (XRD) patterns of CFO and CFOT revealed cubic crystalline spinel structures, which both conformed to the standard pattern of CoFe<sub>2</sub>O<sub>4</sub> (JCPDS 03-0864) and matched the result of the selected area electron diffraction (SAED) patterns (Fig. 1d and Fig. S2b†). The chemical composition and valence state of CFOT were investigated using X-ray photoelectron spectroscopy (XPS).<sup>51,52</sup> The survey XPS spectrum revealed that CFOT contained Co, Fe, O, N, and S, corresponding to CoFe<sub>2</sub>O<sub>4</sub> and Tf (Fig. 1e). The high-resolution Co 2p XPS spectrum of CFOT showed two typical peaks of Co 2p<sub>1/2</sub> at 796.4 eV (satellite peaks at 802.4 eV) and Co 2p<sub>3/2</sub> at 780.9 eV (satellite peaks at 786.9 eV), which were assignable to Co<sup>2+</sup> (Fig. S4a†). Two peaks at 723.9 eV (satellite peaks at 732.0 eV) and 710.8 eV (satellite peaks at 718.9 eV) were assigned to Fe

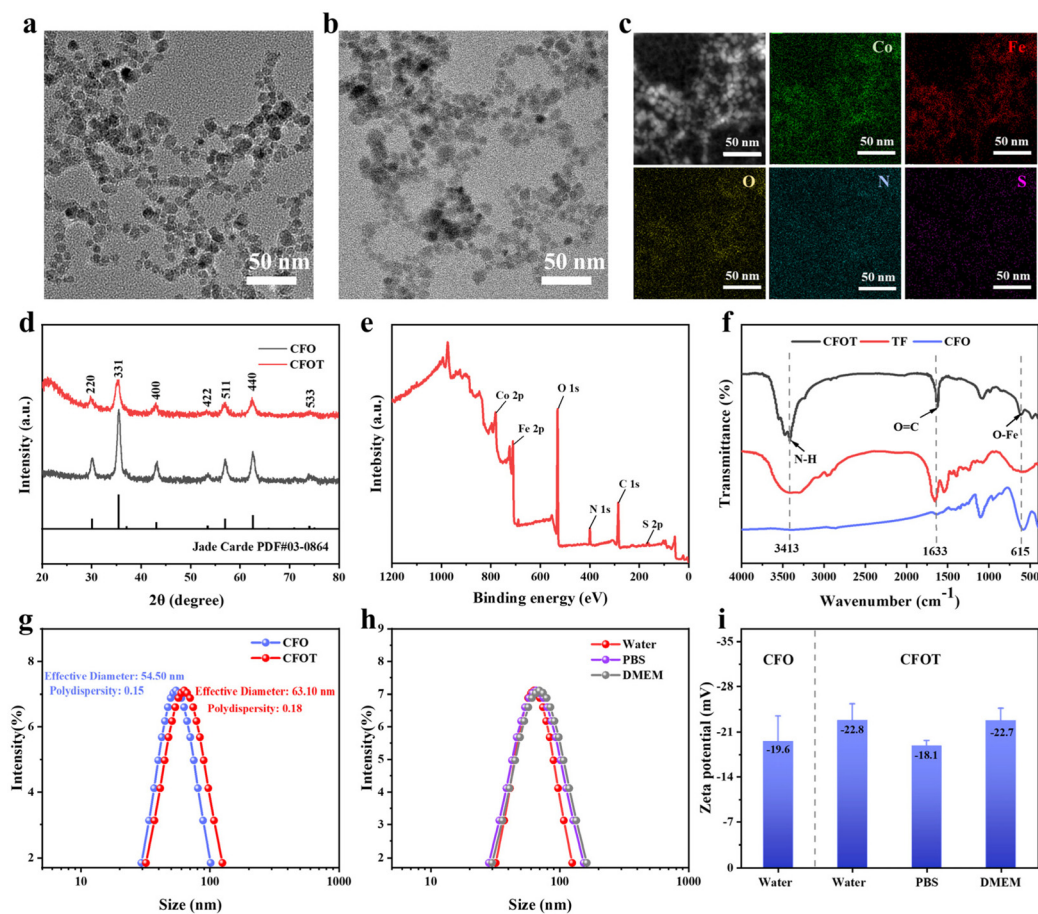


**Fig. 1** Preparation and characterization of CFOT. TEM images of as-synthesized (a) CFO and (b) CFOT. (c) HAADF-STEM image and elemental mapping of Co, Fe, O, N, and S of CFOT. Scale bar: 50 nm. (d) XRD patterns for the prepared CFO and CFOT and corresponding standard PDF card. (e) Survey XPS spectrum of CFOT. (f) FT-IR spectra of CFO, Tf, and CFOT. (g) Hydrodynamic diameter distribution of CFO and CFOT in aqueous solution, and (h) hydrodynamic size of CFOT in water, PBS, and DMEM. (i) Surface zeta potentials of CFO in water and CFOT in water, PBS, and DMEM.

2p<sub>1/2</sub> and Fe 2p<sub>3/2</sub>, respectively, demonstrating the existence of Fe<sup>3+</sup> (Fig. S4b†). Peaks at 529.9 eV and 531.3 eV were attributed to O<sup>2-</sup> (Fig. S4c†). Inductively coupled plasma mass spectrometry (ICP-MS) characterization demonstrated that the mass percentages of CoFe<sub>2</sub>O<sub>4</sub> in CFO and CFOT were 14.85% and 13.55%, respectively (Table S1†). The binding of Tf and CFO was demonstrated by Fourier transform infrared (FT-IR) spectroscopy with the absorption peaks at 3413 cm<sup>-1</sup> (stretching vibration of N-H) and 1633 cm<sup>-1</sup> (stretching vibration of O=C) of Tf and the absorption peak at 615 cm<sup>-1</sup> (symmetric stretching vibration of O-Fe) in the CFOT (Fig. 1f).<sup>53,54</sup> After detection by dynamic light scattering (DLS), the equivalent hydrodynamic size of CFOT was determined to be ~63.10 nm in the aqueous solution, which was slightly higher than that of CFO (~54.50 nm) (Fig. 1g) with minor variations in other solutions (PBS, DMEM) (Fig. 1h). Also, the CFOT still showed a negative potential (-22.80 mV) after loading with Tf (Fig. 1i). Furthermore, the tremendous stability and dispersibility of CFOT were demonstrated by the slight variation in hydrodynamic size, zeta potential, and polydispersity within 7 days (Fig. S5a-c†). The CFOT had excellent solution stability and

biocompatibility by using mPEG-P(AGE-MPA) as a stabilizer and by the modification of Tf. The above results demonstrated that the successfully constructed CFOT possessed the properties of a small particle size, negative charge, and high stability, which would support the application of CFOT in antitumor drugs.

## 2.2. Photophysical properties of CFOT

As presented in the UV-Vis-NIR absorption spectrum (Fig. 2a), the CFOT nanoparticles exhibited a broad NIR absorption band in the wavelength range of 650–850 nm. The absorption of CFOT at 808 nm grew as the concentration increased, indicating the tremendous potential of CFOT as an active photothermal agent in the NIR window. An 808 nm laser (1.2 W cm<sup>-2</sup>) was used to irradiate CFOT at various concentrations for 10 min, with deionized water serving as a blank control. Utilizing a thermal infrared camera to capture photographs, it was discovered that the increase in temperature was dependent on the irradiation time and concentration (Fig. 2b). After 10 min of irradiation, the temperature increased to 61.4 °C at the CFOT concentration of 400 μg mL<sup>-1</sup>, although the water

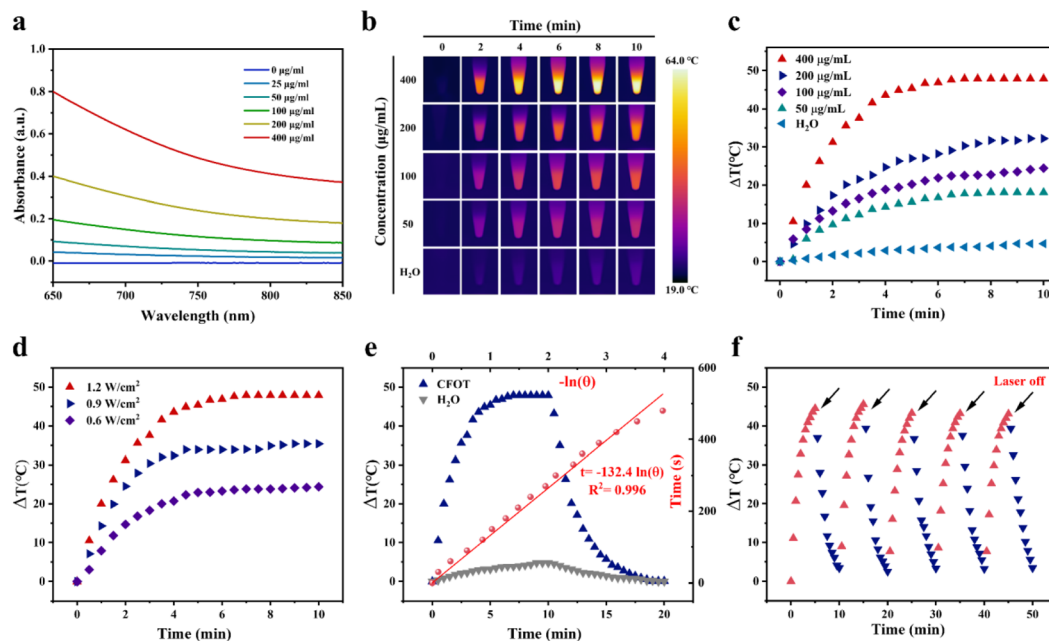


**Fig. 2** Photothermal performance of CFOT. (a) UV absorbance of CFOT with different concentrations. (b) Thermal imaging of CFOT at different concentrations. Temperature variation curves *versus* time of CFOT with (c) different concentrations and (d) different laser powers under 808 nm laser irradiation. (e) Temperature changes of water and CFOT under the condition of the laser switched on and off. (f) Temperature changes of CFOT for five laser on/off cycles.

temperature only increased by 1.2 °C (Fig. 2c). Furthermore, the temperature of the CFOT solutions gradually increased as the power rose. At varied power densities (0.6, 0.9, and 1.2 W cm<sup>-2</sup>), the maximum temperature of the CFOT dispersion was raised by 24.4 °C, 35.4 °C, and 47.9 °C, respectively (Fig. 2d).

As illustrated in Fig. 2e, a plot of the cooling period *versus* the negative log of temperature and time, which was obtained from the cooling period of the curve, was used to calculate the heat-transfer time of  $\tau_s = 132.40$ . The photothermal conversion efficiency ( $\eta$ ) of the CFOT was about 46.5%, indicating that the CFOT could convert NIR laser light into thermal heat energy efficiently. During the five consecutive light heating and natural cooling cycle process, the heating rate and maximum temperature of the CFOT hardly changed obviously, which clarified the favorable photothermal reversibility and cyclic stability of CFOT (Fig. 2f). Therefore demonstrating that CFOT would be an excellent photothermal agent to treat tumors.

### 2.3. GSH depletion and $\cdot$ OH generation of CFOT

A schematic representation of GSH depletion and  $\cdot$ OH production is illustrated in Fig. 3a. GSH, as an ample endogenous antioxidant, demonstrated strong reducibility for scavenging ROS. Thus, the consumption of GSH could improve the killing effect of  $\cdot$ OH on tumor cells by disrupting redox homeostasis. 5,5'-Dithiobis-(2-nitrobenzoic acid) (DTNB) was adopted to detect the depletion of GSH in different concentrations of CFOT and at different time points (0, 10, 30, 60, 90, 120, 150, 180, and 240 min). The DTNB's absorbance peak was reduced over time after adding CFOT to GSH (Fig. 3b). After

reacting for 4 h, the characteristic absorption peak was barely observed, which demonstrated that GSH was almost depleted. Furthermore, a significant decrease in absorption at 412 nm was observed with the increase in CFOT concentration from 25 to 200  $\mu\text{g mL}^{-1}$  over 4 h (Fig. 3c), which demonstrated that CFOT possessed a strong GSH-depletion capacity.

Methylene blue (MB) could be oxidized by highly reactive  $\cdot$ OH accompanied by a fading blue color, which could be detected by UV-visible spectrophotometry at around 664 nm. To evaluate the CDT performance of CFOT nanoparticles, the  $\cdot$ OH generated by the Fenton-like reaction of CFOT and H<sub>2</sub>O<sub>2</sub> was determined by MB assay at pH 6.5. It was observed that the absorbance gradually decreased with the increase in time (Fig. 3d). Apparently, the absorbance of the solution decreased dramatically within 2 h and could be barely observed after 5 h of incubation, indicating that the MB was almost completely degraded. Then, the absorbance of MB was not affected by CFOT, GSH, and H<sub>2</sub>O<sub>2</sub> alone after 2 h of incubation (Fig. 3e). However, the absorbance of the mixed solution decreased substantially after adding H<sub>2</sub>O<sub>2</sub> to the CFOT solution, which demonstrated that CFOT had excellent Fenton catalytic properties. When GSH was added to the mixture of CFOT and H<sub>2</sub>O<sub>2</sub>, another rapid decrease in absorbance was detected, which was attributed to the degradation of CFOT after reacting with GSH and H<sub>2</sub>O<sub>2</sub> (confirmed by TEM, and as shown in Fig. S6†) and the production of large amounts of low-valent Fe<sup>2+</sup> through the reduction of GSH (confirmed by XPS, and as shown in Fig. S7†). In addition, the TMB assays also demon-

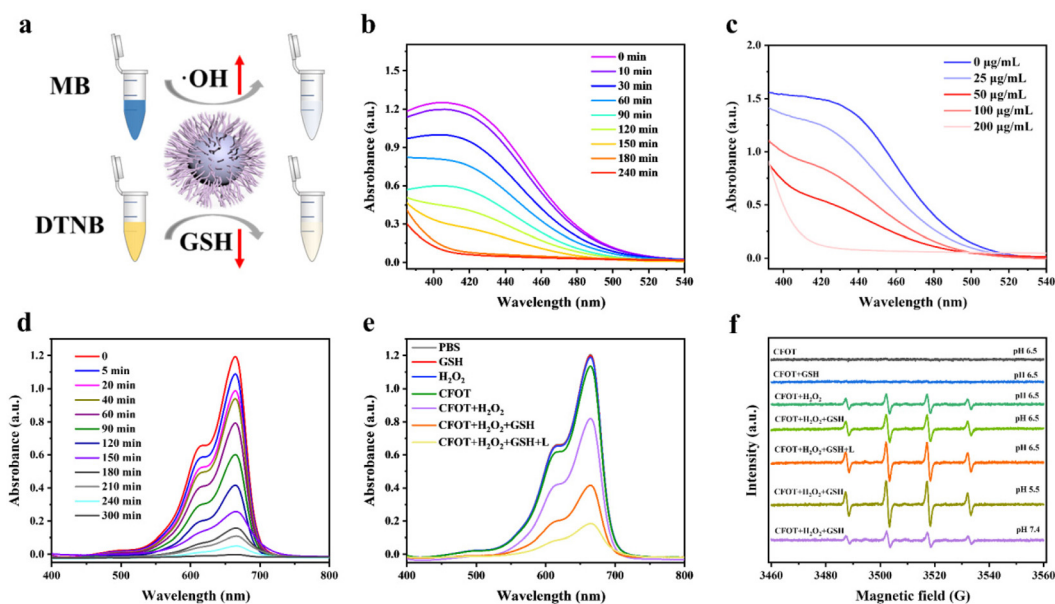


**Fig. 3** GSH depletion and H<sub>2</sub>O<sub>2</sub> production. (a) Schematic representation of the detection of GSH depletion and enhanced  $\cdot\text{OH}$  production. (b) GSH depletion by CFOT at different times, and (c) concentration-dependent GSH depletion by CFOT. Methylene blue (MB) absorption curve of CFOT for (d) different reaction times and (e) different treatment groups. (f) ESR spectra of CFOT in different treatment groups.

strated the Fenton reaction performance of CFOT (Fig. S8†). In addition, a more substantial decrease in absorbance was detected after the addition of irradiation with an 808 nm laser, which indicated that the increase in temperature further accelerated the production of  $\cdot\text{OH}$  by promoting the efficiency of the Fenton or Fenton-like reaction. The  $\cdot\text{OH}$  was further determined by electron spin resonance (ESR) with 5,5-dimethyl-1-pyrroline-*N*-oxide (DMPO) used as a spin trap. In the CFOT group and CFOT + GSH group, the neglected spin signal was observed due to the absence of the Fenton reaction (Fig. 3f). The CFOT + H<sub>2</sub>O<sub>2</sub> group had a signal for a certain amount of hydroxyl radicals at pH 6.5, which was rapidly enhanced by the addition of GSH. Moreover, a stronger  $\cdot\text{OH}$  signal could be observed with 808 nm laser irradiation under pH 6.5 conditions, which was consistent with the above absorbance data. The pH plays a vital role in the Fenton reaction. The  $\cdot\text{OH}$  signal was weak when the pH of the sample was 7.4, while a more significant sign of  $\cdot\text{OH}$  could be observed as the pH decreased to 5.5. Therefore, CFOT has tumor-responsive properties with high safety in normal tissues with neutral and low GSH levels. CFOT achieved multi-enhanced CDT by depleting GSH and synergizing with PTT.

#### 2.4 *In vitro* cell-uptake study

HepG2 cells with abundant transferrin receptors (TfR) were used to probe the targeting ability of Tf to cancer cells with CFOT and CFO labeled with FITC (Fig. S9a and b†). The HepG2 cells cultured with CFOT for 2 h showed significantly stronger green fluorescence than those cultured with CFO without Tf modification *via* confocal laser scanning microscopy (CLSM) observation, which demonstrated that the

modification with Tf increased the uptake of nanodrugs by cancer cells (Fig. 4a and b). In addition, ICP-MS was used to detect the concentrations of the Co element in 2 normal cells (HUVEC and LO-2) and 2 cancer cells (HepG2 and H22) after co-incubation with CFOT for 2 h, respectively. The concentrations of the Co element in H22 and HepG2 cells were significantly higher than those in HUVEC and LO-2, which indicated a higher uptake of CFOT by tumor cells than that by normal cells (Fig. 4c). These results suggested that the targeted modification of Tf endowed CFOT nanoparticles with efficient drug-delivery properties to tumor cells to improve the therapeutic effect and reduce the damage to normal cells.

#### 2.5 *In vitro* cytotoxicity assay and synergistic therapeutic performance

The cell viability of HUVEC cells and LO-2 cells treated with CFO and CFOT was assessed *via* a standard methyl thiazolyl tetrazolium (MTT) assay. As presented in Fig. 5a, the survival of HUVEC and LO-2 presented a negligible decrease with increasing concentrations after 24 h of co-incubation with CFOT and could be maintained at around 80% even when the concentration was as high as 400 µg mL<sup>-1</sup>. CFO also did not significantly inhibit the growth of the two cells under the same treatment conditions, which could be attributed to the enhancement of the stability by mPEG-P(AGE-MPA), the low cellular uptake, and the absence of acidity in the cells micro-environment. Therefore, CFOT and CFO exhibited low toxicity to normal cells and high biocompatibility.

CFO and CFOT had a certain cytotoxicity on tumor cells (H22 and HepG2). CFOT caused a concentration-dependent

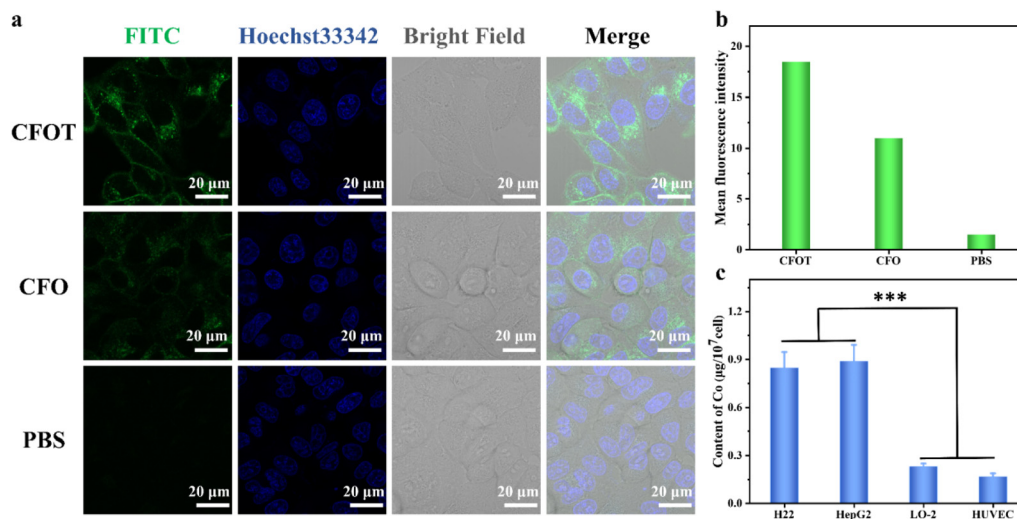


**Fig. 4** Cellular uptake assay. (a) CLSM images of HepG2 cells treated with FITC-labeled CFO and CFOT and (b) corresponding average fluorescence intensities of the different groups; scale bar: 20  $\mu\text{m}$ . (c) Detection of the uptake capability of different cells (H22, HepG2, LO-2, and HUVEC) to CFOT by ICP-MS. \*\*\* $p < 0.001$ , \*\* $p < 0.01$ , or \* $p < 0.05$ .

decrease in viability of HepG2 or H22 cells with variable concentrations from 25 to 400  $\mu\text{g mL}^{-1}$  (Fig. 5b and c). Also, the mortality of HepG2 cells and H22 cells reached about 38.3% and 37.5% under treatment with CFOT at 400  $\mu\text{g mL}^{-1}$ , which was caused by CDT alone. Under NIR laser irradiation, CFOT exhibited more significant tumor toxicity than without the laser irradiation. Compared to the CFOT group, the survival rate of cells in the CFOT + L group decreased by varying degrees at all concentrations after being irradiated with an 808 nm laser (1.2  $\text{W cm}^{-2}$ , 10 min), with the survival rate of the cells at the highest concentration being only about 13%. The growth of HepG2 and H22 was partially inhibited by CFO, while there was no significant difference between the toxicity of the CFO group and CFO + L group on the cells. Apparently, the inhibition of tumor cell growth by CFO was lighter than that by CFOT, which was primarily attributed to the decreased cellular uptake due to the absence of Tf targeting modifications. Overall, the MTT results on tumor cells showed that the PTT/CDT synergistic therapy of CFOT had excellent antitumor performance compared to monotherapy.

The mutually reinforced PTT/CDT synergistic effect of CFOT was also demonstrated *via* a calcein AM and propidium iodide (PI) co-staining assay (Fig. 5d). The HepG2 tumor cells in the CFO group demonstrated no significant decrease in cell viability. Whereas CFOT or CFO + L exhibited a partial HepG2 cell-killing effect due to the synergistic effect of CDT and PTT or single CDT with targeted enhancement. Significantly, an intense red fluorescence of PI was observed in the CFOT + L group, indicating that almost all the cancer cells were dead, which was consistent with the MTT test results. To further demonstrate the *in vitro* tumor apoptosis-induced ability of CFOT, Annexin V-FITC/PI apoptosis staining was performed (Fig. 5e). Only a small proportion of the cells were dispersed in the apoptotic region in the CFO group. HepG2 cells showed

partial apoptosis after incubation with CFO under irradiation and CFOT only. Cell apoptosis occurred in both the early and late stages with remarkable increments in the case of CFOT under irradiation, indicating the effective synergistic PTT/CDT performance.

The generation of intracellular ROS was detected by CLSM using the fluorescent probe of 2',7'-dichlorofluorescein diacetate (DCFH-DA), which could produce green fluorescence after being oxidized by ROS. Due to the presence of a minor amount of  $\cdot\text{OH}$ , HepG2 cancer cells treated with CFO showed mild green fluorescence. CFOT exhibited a stronger fluorescence signal than CFO under the targeted enhancement effect. In addition, the green fluorescence of the CFO + L group was more potent than for the CFO group under 808 nm laser irradiation. The CFOT + L group exhibited the highest level of ROS production, suggesting that heat therapy enhanced CDT (Fig. 5f). GSH possessed a certain inhibitory capacity for ROS-mediated CDT due to its reducing ability, and so the intracellular GSH depletion capacity of the nanoparticles was measured by a GSH assay kit. The GSH in cells could be effectively depleted in the presence of CFOT and CFO (Fig. 5g). Clearly, CFOT had a more remarkable ability to deplete GSH, which would further promote CDT.

Compared with other materials, CFOT had excellent Fenton, GSH depletion, and photothermal properties, and exhibited high stability and biosafety after using mPEG-P (AGE-MPA) as a stabilizer. In addition, the modification of transferrin gave CFOT a tumor-specific targeting ability that is not available in general nanomaterials, and thus CFOT showed efficient PTT/CDT antitumor efficacy.

## 2.6 Treatment mechanism of the synergistic PTT/CDT

ROS generated through the reaction of CFOT with  $\text{H}_2\text{O}_2$  may cause the lipid peroxidation (LPO) of biological membranes,

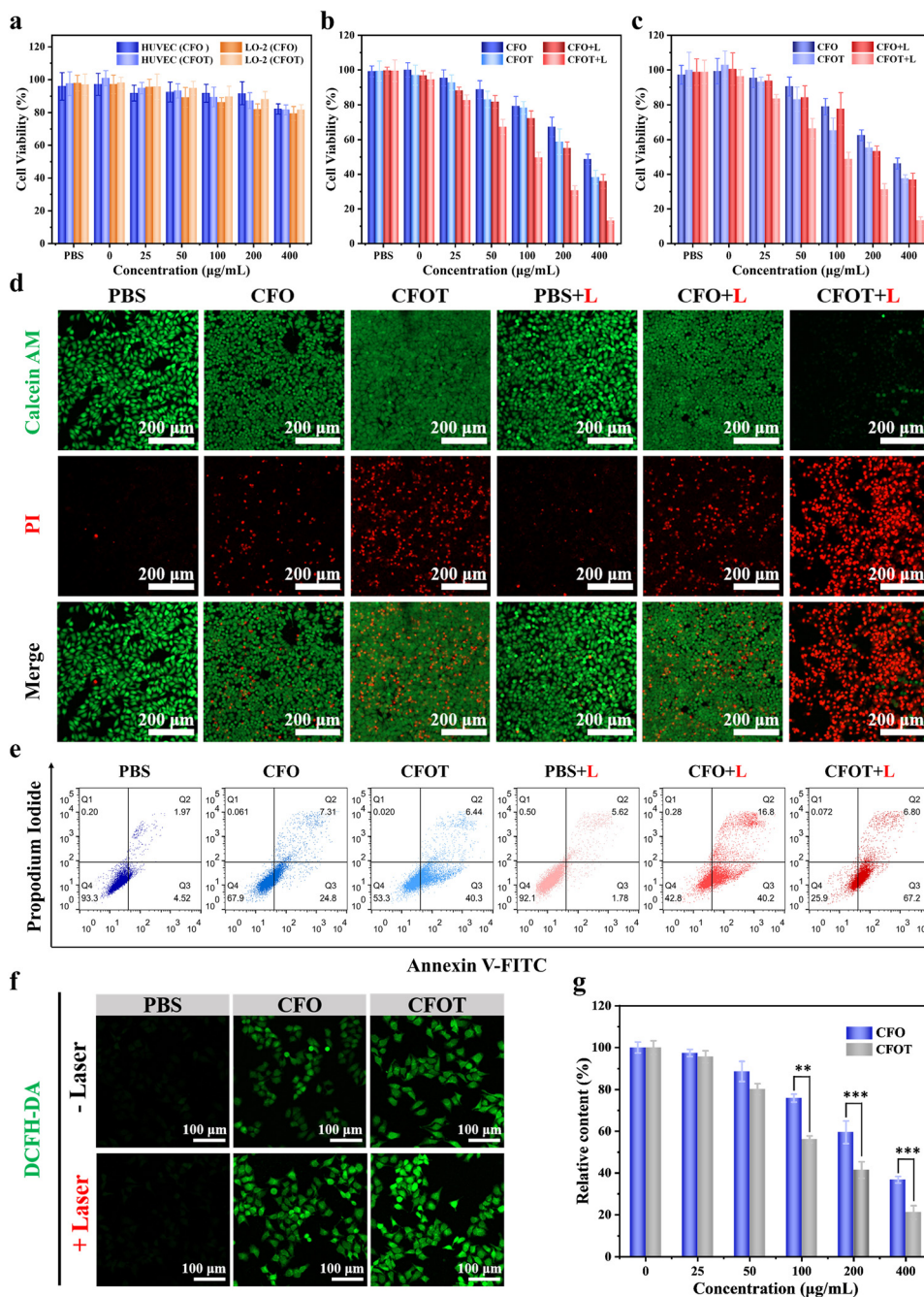


**Fig. 5** (a) Relative cell viabilities of HUVEC and LO-2 cells after 24 h incubation with CFO and CFOT at different concentrations by MTT assay. Relative cell viability of (b) HepG2 cells and (c) H22 cells treated with CFO, CFOT, CFO + L, and CFOT + L by MTT assay, L: 808 nm,  $1.2 \text{ W cm}^{-2}$ , 10 min (d) CLSM images of HepG2 cells stained with calcein AM and PI after different treatments (PBS, CFO, CFOT, PBS + L, CFO + L, and CFOT + L); scale bar: 200  $\mu\text{m}$ . (e) Flow cytometric apoptosis analysis of Annexin V-FITC/PI-stained HepG2 cells after different treatments. (f) CLSM images of HepG2 cells in the detection of  $\cdot\text{OH}$  using DCFH-DA as a probe after various treatments; scale bar: 100  $\mu\text{m}$ . (g) Analysis of the relative GSH levels of HepG2 cells in the treatment groups CFO and CFOT + L. \*\*\* $p < 0.001$ , \*\* $p < 0.01$ , or \* $p < 0.05$ .

which can severely damage cellular organelles (such as mitochondria and lysosomes). To elucidate CFOT-triggered lipid peroxidation, the C11-BODIPY<sup>581/591</sup> fluorescent probe, which emits green fluorescence in the presence of lipid peroxidation, was employed to examine the LPO occurring in HepG2 cells treated with different groups (Fig. 6a). The CLSM images

showed that HepG2 cells in the CFO group presented weaker green fluorescence than that of the CFOT group after C11-BODIPY<sup>581/591</sup> staining. This green fluorescence was further enhanced under 808 nm laser irradiation. The CFOT + L group showed the strongest green fluorescence, successfully demonstrating the ability of CFOT to elicit PTT-enhanced LPO. In

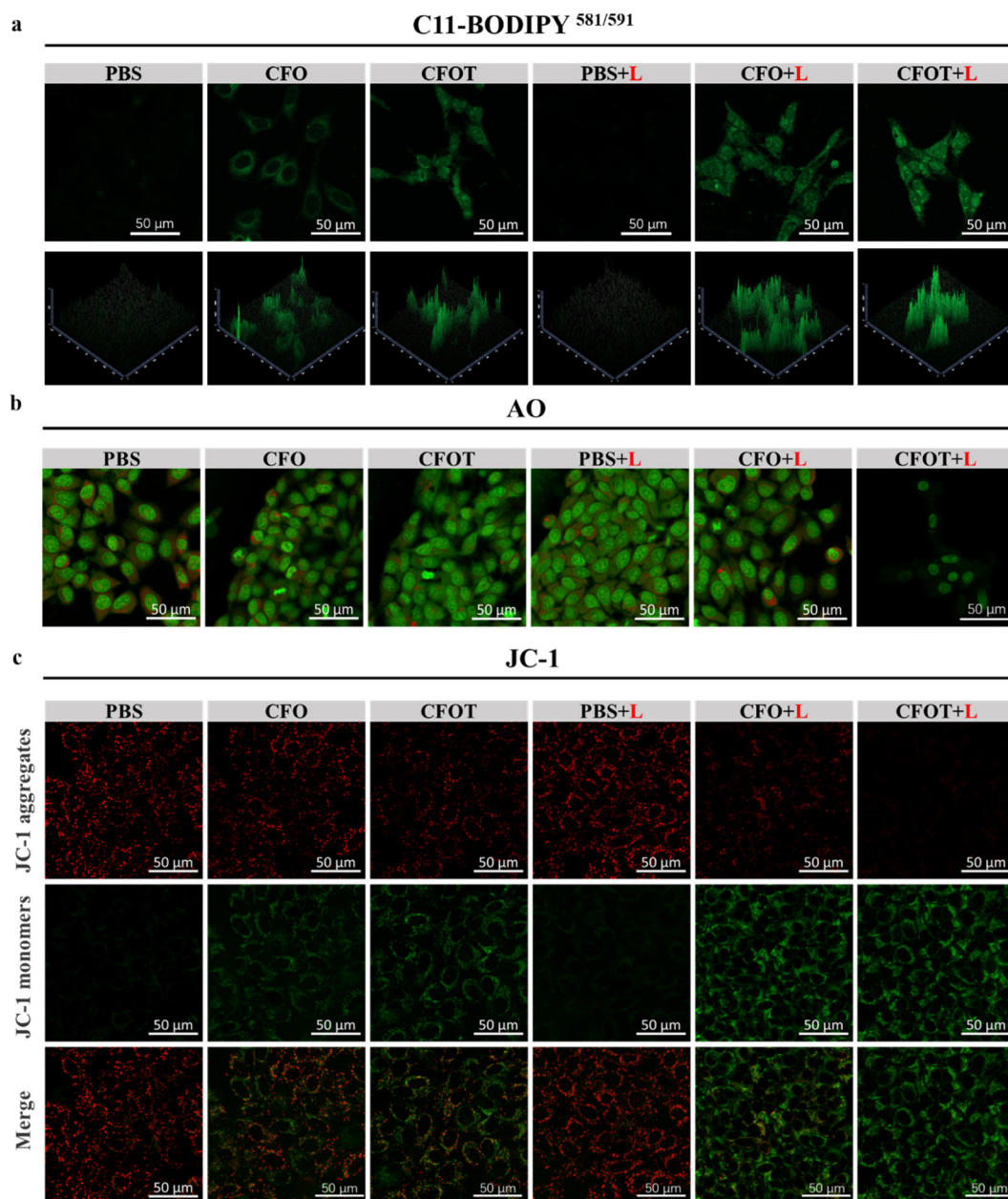


**Fig. 6** (a) CLSM images of C11-BODIPY<sup>581/591</sup>-stained HepG2 cells treated with different groups (containing PBS, PBS + CFO, CFOT CFO + L, and CFOT + L) to detect intracellular lipid peroxidation (LPO). (b) CLSM images of AO-stained HepG2 cells incubated with different groups. (c) Mitochondrial membrane potential changes of HepG2 cells treated with different groups detected by the JC-1 kit presented in the CLSM images. Scale bar: 50  $\mu$ m.

addition, the hyperthermia generated by CFOT under 808 nm laser caused irreversible damage to cell organelles.

We initially researched the damage from different treatments to lysosomes by PTT and CDT. The acridine orange (AO) staining assay was used to evaluate the lysosomal membrane permeabilization (LMP) of HepG2 cells. As shown in Fig. 6b, the red fluorescence of the whole cytoplasm was gradually reduced after treatment with PBS, PBS + L, CFO, CFO + L, CFOT, and CFOT + L. The red fluorescence was greatly diminished upon treatment with CFOT + L in HepG2 cells,

suggesting that CFOT generated the most severe damage to the lysosome through the targeting-enhanced synergy of CDT and PTT. Then, 5,5',6,6'-tetrachloro-1,1',3,3'-tetraethyl-imidacarbocyanine iodide (JC-1) was used to detect the changes in mitochondrial membrane potential (MMP) to assess the mitochondrial damage caused by PTT and CDT. HepG2 cells treated with CFO showed a little lowering of the red fluorescence and the appearance of green fluorescence in comparison to the control group (Fig. 6c). The MMP of HepG2 cells treated with CFO + L and CFOT showed significant decreases. The CFOT +



L group had the most extreme depolarization of mitochondrial membranes, as demonstrated by the increased green fluorescence and elimination of red fluorescence in the cells, suggesting that the synergistic effect of PTT and CDT of CFOT dramatically promoted mitochondrial failure. These experimental results revealed that the CDT-generated  $\cdot\text{OH}$  and PTT-induced local hyperthermia could cause a severe rupture of lysosomes and induce mitochondria dysfunction. Lysosomal damage would cause a release of numerous proteolytic enzymes (such as caspases), which are essential for activating cancer-cell apoptosis. Mitochondrial dysfunction can result in mitochondrial hypertonicity, directly leading to cell apoptosis. The CDT/PTT synergistic therapy of CFOT achieved mutually enhanced tumor therapeutic effects through lysosomal damage and mitochondrial dysfunction under NIR irradiation.

### 2.7 *In vivo* targeting performance of CFOT

The *in vivo* performance of CFOT was investigated using the H22 subcutaneous tumor model of Balb/c mice. All the animal procedures were performed in accordance with the Guidelines for Care and Use of Laboratory Animals of Guangdong University of Technology and approved by the Animal Ethics Committee of Guangdong University of Technology. Considering the apparent specific cell-uptake performance of CFOT to liver cancer cells *in vitro*, we further investigated the tumor-targeting capability of CFOT by thermal imaging and by detecting the concentration of Co at the tumor site. Photothermal imaging of the tumor-bearing mice treated with PBS, CFO, or CFOT through tail vein injection was performed by NIR thermography under 808 nm laser irradiation ( $1.2 \text{ W cm}^{-2}$ , 10 min). Different intravenous injection time points were designed to explore the optimal timing of irradiation and tumor targeting. The tumor temperature gradually became higher, with the highest temperature being  $49.5 \text{ }^\circ\text{C}$  at 12 h after intravenous injection in the CFO-treated tumor-bearing mice group (Fig. 7a, S10 and S11<sup>†</sup>). However, the tumor temp-

erature of the tumor-bearing mouse treated with CFOT showed a noticeable increase at 5 h post-injection, compared with the CFO treatment group. The tumor temperature within the tumor tissue continued to increase and was suddenly strengthened at 8 h post-injection, with the highest temperature of  $59.6 \text{ }^\circ\text{C}$ , and then maintained stability at 12 h post-injection before showing a slow decline at 24 h post-injection. These experimental results demonstrated that CFOT had a better tumor targeting ability than CFO, and that the optimal radiation time points for CFOT and CFO were 8 and 12 h after intravenous injection, respectively. Then, the concentration of the Co element in the tumor was detected *via* ICP-MS, which demonstrated the more efficient tumor enrichment of tumor-bearing mice treated with CFOT at 8 h after intravenous injection and the optimal time of CFO aggregation at the tumor site at 12 h after intravenous injection (Fig. 7b). In addition, the concentration of the Co element in the tumors of CFOT-treated tumor-bearing mice were generally higher than in the CFO group, which was consistent with the thermal imaging data, further confirming the excellent special targeting ability of CFOT *in vivo*.

### 2.8 *In vivo* synergistic therapeutic performance

The anticancer effect of CFOT *in vivo* was further investigated using the H22 tumor-bearing mice model. The tumor-bearing mice with a tumor volume of  $100 \text{ mm}^3$  were assigned to six groups (five mice per group) randomly for various treatments: (1) injected PBS (PBS group, control group), (2) injected CFO (CFO group), (3) injected CFOT (CFOT group), (4) injected PBS and irradiated with an 808 nm laser (PBS + L group), (5) injected CFO and irradiated with an 808 nm laser (CFO + L group), and (6) injected CFOT upon 808 nm laser irradiation (CFOT + L group).

A schematic diagram of the tumor-treatment procedure is presented in Fig. 8a. All the treatments were performed with only one injection and the NIR laser performed single radi-

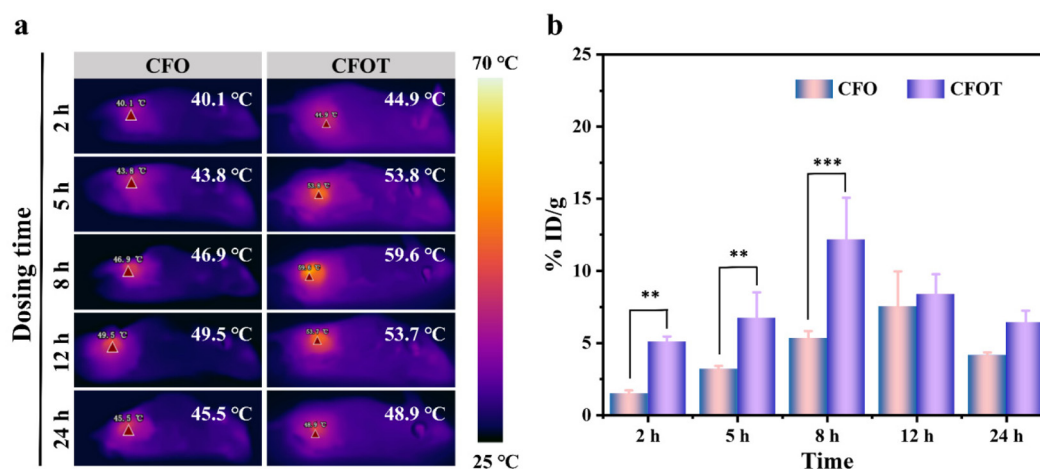
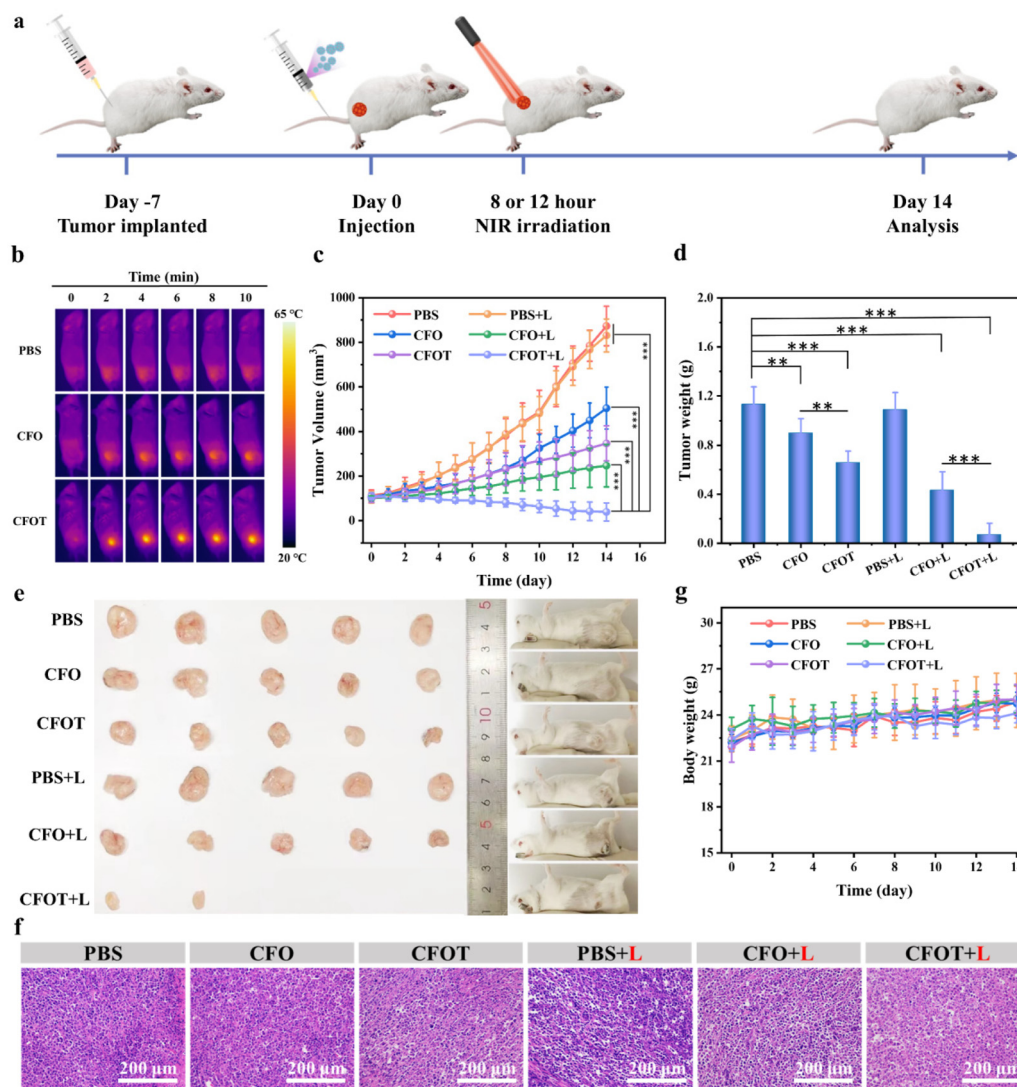


Fig. 7 (a) Thermal imaging of CFO and CFOT under different administration time conditions in H22 tumor-bearing mice. (b) The Co concentrations in tumor sites of H22 tumor-bearing mice treated with CFO and CFOT at different intravenous injection time points. \*\*\* $p < 0.001$ , \*\* $p < 0.01$ , or \* $p < 0.05$ .



**Fig. 8** *In vivo* synergistic anticancer efficacy. (a) Schematic diagram of the *in vivo* anti-cancer treatment process in tumor-bearing mice. (b) IR thermal images of H22-tumour-bearing mice injected with PBS, CFO, and CFOT under 808 nm laser ( $1.2 \text{ W cm}^{-2}$ ) irradiation. (c) Relative tumor-volume growth curves of different treatment groups, and (d) mean tumor weight of different treatment groups. (e) Representative photographs of resected tumors and corresponding mice pictures in different treatment groups. (f) H&E staining of tumor sections of tumor-bearing mice treated with different treatment groups. (g) Body weight changes in mice after various treatments during treatment. Scale bar: 200  $\mu\text{m}$ . \*\*\* $p < 0.001$ , \*\* $p < 0.01$ , or \* $p < 0.05$ .

ation for the optimal exposure time (CFO at 12 h and CFOT at 8 h after intravenous injection, respectively). According to these thermal images, the tumor-site temperature reached 50 °C promptly within 2 min irradiation and kept a temperature above 57 °C after 5 min in the CFOT + L group, which could effectively ablate tumors (Fig. 8b). The temperature in the tumor area of the PBS + L group was increased by 41.5 °C. Also, the local tumor temperature of the CFO + L group slowly rose to 54 °C, which was significantly weaker than that of CFOT.

The relative tumor volumes of the H22 tumor-bearing mice were measured every day for 14 days observation. As shown in Fig. 8c, the tumor volumes of the PBS group and PBS + L group grew uncontrollably, while the CFO group showed

partial tumor inhibition under CDT treatment. The tumor volumes of CFO + L and CFOT grew more slowly compared with those treated with PBS and CFO, which was ascribed to the PTT strengthening CDT and tumor targeting, respectively. Notably, the tumor exhibited the best tumor inhibition and it even disappeared in the CFOT + L group due to the targeting effect of Tf and the synergistic therapy of PTT and CDT, confirming the remarkable PTT/CDT synergistic tumor destruction effect with the targeted enhancement of Tf. The tumor weight indicated that CFOT + L caused severe damage to the tumor tissue, with the lowest tumor weight being under CDT/PTT synergistic treatment, while the CFO, CFO + L, and CFOT groups showed partial inhibition compared with the control group (Fig. 8d). The corresponding morphology of the excised

tumors and corresponding H22 tumor-bearing mice pictures are presented in Fig. 8e. The CFO, CFOT, and CFO + L groups showed a progressive decrease in tumor size and a certain tumor growth inhibition. The tumor of CFOT + L was significantly reduced and some of the mice had been completely cured, which was in agreement with the results of tumor volume. Moreover, Histological analysis (H&E) of tumor tissue slices confirmed the tumor treatment effect of CFOT (Fig. 8f).

To evaluate the potential toxicity of CFOT *in vivo*, the blood routine and biochemical indexes analysis of tumor-bearing mice after treatment was performed. No significant differences were observed in the blood biochemical analysis among all the groups. The results confirmed that the influence of the nano-platform on the liver and kidney functions was negligible (Fig. S12†). H&E examination of the major organs (such as heart, liver, spleen, lungs, and kidneys) presented insignificant pathological toxicity and inflammatory lesions, demonstrating the good biocompatibility (Fig. S13†). Furthermore, the body weight of the mice in the six groups presented an increasing trend throughout the treatment period (Fig. 8g), indicating the negligible side effects of CFOT. The *in vivo* antitumor results demonstrated that CFOT could effectively treat liver tumors through the synergistic effects of PTT and CDT with a high biosafety profile.

### 3. Conclusion

In conclusion, we successfully fabricated a novel multifunctional CoFe<sub>2</sub>O<sub>4</sub>@Transferrin (CFOT) nanoparticle, which could effectively target cancer cells and consume endogenous GSH to reduce the resistance of cancer cells to intracellular oxidative stress and enhance the CDT effect, thereby dramatically improving the biosafety and the therapeutic efficiency of CDT/PTT. The different uptake of CFOT by cancer cells and normal cells was confirmed by CLSM and ICP-MS, and the effective accumulation at the H22-bearing mice tumor site further confirmed the particular tumor targeting of CFOT. Meanwhile, CFOT presented an excellent photothermal effect under the irradiation of an 808 nm laser and the Fenton reaction was further accelerated by the warming up, resulting in a significant improvement of PTT/CDT. The ROS/photothermal-induced cell apoptosis mechanism of the nanoparticles was proved by CLSM. *In vitro* and *in vivo* treatment results showed that, through the synergistic CDT/PTT treatment of CFOT, the apoptosis rate of HepG2 and H22 cells was up to 87%, and the H22 tumor was almost completely ablated without significant systemic toxicity during the treatment period. Therefore, the “all-in-one” nanoparticles could not only effectively deliver nanomedicines to targeted tumors, avoiding the potential damage to normal tissues, but could also realize GSH depletion/heat-enhanced CDT/PTT for highly efficient cancer therapy. The designed novel multifunctional nanoparticles provide a promising strategy for safe and efficient tumor treatment and clinical translation in the future.

### Author contributions

Liu X., He Y. designed the study and supervised the project; Chen N., Wang Y., and Zeng Y. conceived the experimental scheme, performed the experiments, and characterized the samples; Chen N., Li Y., Pan Z., and Li H. carried out the *in vitro* and *in vivo* experiments; Chen J., Chen Z. and Yuan J. performed data analysis; Chen N. wrote the paper with support from Yan W., Lu Y. and Zhang K. All authors contributed to the general discussion.

### Conflicts of interest

The authors declare no competing financial interest.

### Acknowledgements

This research was supported by the National Natural Science Foundation of China (Grant No. 81803000 & 32171314), Guangdong Basic and Applied Basic Research Foundation (2022A1515010671), Guangzhou Basic and Applied Basic Research Foundation (202201010371), and University Innovative Team Support for Major Chronic Diseases and Drug Development (26330320901).

### References

- 1 H. Sung, J. Ferlay, R. L. Siegel, M. Laversanne, I. Soerjomataram, A. Jemal and F. Bray, *CA Cancer J. Clin.*, 2021, **71**, 209–249.
- 2 C. Xia, X. Dong, H. Li, M. Cao, D. Sun, S. He, F. Yang, X. Yan, S. Zhang, N. Li and W. Chen, *Chin. Med. J.*, 2022, **135**, 584–590.
- 3 J. Ferlay, M. Colombet, I. Soerjomataram, D. M. Parkin, M. Pineros, A. Znaor and F. Bray, *Int. J. Cancer*, 2021, **149**, 778–789.
- 4 X. Nie, L. Xia, H. L. Wang, G. Chen, B. Wu, T. Y. Zeng, C. Y. Hong, L. H. Wang and Y. Z. You, *ACS Appl. Mater. Interfaces*, 2019, **11**, 31735–31742.
- 5 P. Wang, X. Wang, Q. Luo, Y. Li, X. Lin, L. Fan, Y. Zhang, J. Liu and X. Liu, *Theranostics*, 2019, **9**, 369–380.
- 6 O. M. Ozpiskin, L. Zhang and J. J. Li, *Theranostics*, 2019, **9**, 1215–1231.
- 7 M. Chen, Z. Huang, M. Xia, Y. Ding, T. Shan, Z. Guan, X. Dai, X. Xu, Y. Huang, M. Huang and C. Zhao, *J. Controlled Release*, 2022, **341**, 351–363.
- 8 H. Liu, M. Zhang, H. Jin, K. Tao, C. Tang, Y. Fan, S. Liu, Y. Liu, Y. Hou and H. Zhang, *ACS Biomater. Sci. Eng.*, 2022, **8**, 502–511.
- 9 B. Yang, S. Zhou, J. Zeng, L. Zhang, R. Zhang, K. Liang, L. Xie, B. Shao, S. Song, G. Huang, D. Zhao, P. Chen and B. Kong, *Nano Res.*, 2020, **13**, 1013–1019.
- 10 N. Yang, T. Zhang, C. Cao, G. Mao, J. Shao, X. Song, W. Wang, X. Mou and X. Dong, *Nano Res.*, 2022, **15**, 2235–2243.

- 11 W. Zeng, H. Zhang, Y. Deng, A. Jiang, X. Bao, M. Guo, Z. Li, M. Wu, X. Ji, X. Zeng and L. Mei, *Chem. Eng. J.*, 2020, **389**, 124494.
- 12 D. Zhi, T. Yang, J. O'Hagan, S. Zhang and R. F. Donnelly, *J. Controlled Release*, 2020, **325**, 52–71.
- 13 C. Zhang, H. Pan, X. Wang and S. K. Sun, *Biomater. Sci.*, 2018, **6**, 2750–2756.
- 14 W. Bian, Z. Pan, Y. Wang, W. Long, Z. Chen, N. Chen, Y. Zeng, J. Yuan, X. Liu, Y. J. Lu, Y. He and K. Zhang, *Bioorg. Chem.*, 2021, **113**, 104954.
- 15 X. Ye, X. Liang, Q. Chen, Q. Miao, X. Chen, X. Zhang and L. Mei, *ACS Nano*, 2019, **13**, 2956–2968.
- 16 C. W. Hsiao, E. Y. Chuang, H. L. Chen, D. Wan, C. Korupalli, Z. X. Liao, Y. L. Chiu, W. T. Chia, K. J. Lin and H. W. Sung, *Biomaterials*, 2015, **56**, 26–35.
- 17 X. Chang, M. Zhang, C. Wang, J. Zhang, H. Wu and S. Yang, *Carbon*, 2020, **158**, 372–385.
- 18 Y. Xi, X. Xie, Y. Peng, P. Liu, J. Ding and W. Zhou, *Nanoscale*, 2021, **13**, 5125–5135.
- 19 L. Kong, F. Yuan, P. Huang, L. Yan, Z. Cai, T. Lawson, W. Wu, S. Chou and Y. Liu, *Small*, 2020, **16**, e2004161.
- 20 K. Xu, X. Wu, Y. Cheng, J. Yan, Y. Feng, R. Chen, R. Zheng, X. Li, P. Song, Y. Wang and H. Zhang, *Nanoscale*, 2020, **12**, 23159–23165.
- 21 A. Li, Q. Zhang, S. Zhao, Y. Chong, P. Wu, Y. Li, X. Jin, G. Chen, Y. Qiu, S. Yang and D. Ye, *Nano Res.*, 2022, **15**, 7071–7080.
- 22 L. Zhang, Z. Yang, J. Ren, L. Ba, W. He and C.-Y. Wong, *Nano Res.*, 2020, **13**, 1389–1398.
- 23 J. Xin, C. Deng, O. Aras, M. Zhou, C. Wu and F. An, *J. Nanobiotechnol.*, 2021, **19**, 192.
- 24 L. Zhang, C. X. Li, S. S. Wan and X. Z. Zhang, *Adv. Healthc. Mater.*, 2022, **11**, e2101971.
- 25 T. Hu, L. Yan, Z. Wang, W. Shen, R. Liang, D. Yan and M. Wei, *Chem. Sci.*, 2021, **12**, 2594–2603.
- 26 Y. Yang, P. Wang, R. Shi, Z. Zhao, A. Xie, Y. Shen and M. Zhu, *Chem. Eng. J.*, 2022, **441**, 136042.
- 27 X. Yang, S. Guo, L. Wang, S. Guan, S. Zhou and J. Lu, *Nano Res.*, 2022, **15**, 8228–8236.
- 28 Y. He, S. Guo, Y. Zhang, Y. Liu and H. Ju, *Biomaterials*, 2021, **275**, 120962.
- 29 G. Liu, J. Zhu, H. Guo, A. Sun, P. Chen, L. Xi, W. Huang, X. Song and X. Dong, *Angew. Chem., Int. Ed.*, 2019, **58**, 18641–18646.
- 30 S. Dong, Y. Dong, T. Jia, F. Zhang, Z. Wang, L. Feng, Q. Sun, S. Gai and P. Yang, *Chem. Mater.*, 2020, **32**, 9868–9881.
- 31 C. He, X. Zhang, C. Chen, X. Liu, Y. Chen, R. Yan, T. Fan, Y. Gai, R. J. Lee, X. Ma, J. Luo, Y. Lu, T. Yang and G. Xiang, *Acta Biomater.*, 2021, **122**, 354–364.
- 32 Y. Qi, S. Ren, J. Ye, Y. Tian, G. Wang, S. Zhang, L. Du, Y. Li, Y. Che and G. Ning, *Acta Biomater.*, 2022, **143**, 445–458.
- 33 X.-R. Li, B. Yin, L. Gao, X. Li, H. Huang, G. Song and Y.-G. Zhou, *Nano Res.*, 2022, **15**, 8291–8303.
- 34 J. Chen, Y. Cao, S. Lin, H. Niu, H. Zhang, L. Guan, C. Shu, A. Wu, Y. Bian and Y. Zhu, *Chem. Eng. J.*, 2021, **431**, 133466.
- 35 W. X. Zhang, Y. N. Hao, Y. R. Gao, Y. Shu and J. H. Wang, *ACS Appl. Mater. Interfaces*, 2021, **13**, 38127–38137.
- 36 M. Ou, C. Lin, Y. Wang, Y. Lu, W. Wang, Z. Li, W. Zeng, X. Zeng, X. Ji and L. Mei, *J. Controlled Release*, 2022, **345**, 755–769.
- 37 L. Wang, Y. Xu, C. Liu, W. Si, W. Wang, Y. Zhang, L. Zhong, X. Dong and Y. Zhao, *Chem. Eng. J.*, 2022, **438**, 135567.
- 38 X. Li, E. C. Montague, A. Pollinzi, A. Lofts and T. Hoare, *Small*, 2022, **18**, e2104632.
- 39 X. Qi, G. Wang, P. Wang, Y. Pei, C. Zhang, M. Yan, P. Wei, G. Tian and G. Zhang, *ACS Appl. Mater. Interfaces*, 2022, **14**, 7659–7670.
- 40 J. Y. Yhee, S. J. Lee, S. Lee, S. Song, H. S. Min, S. W. Kang, S. Son, S. Y. Jeong, I. C. Kwon, S. H. Kim and K. Kim, *Bioconjugate Chem.*, 2013, **24**, 1850–1860.
- 41 M. Qasim, K. Asghar and D. Das, *Ceram. Int.*, 2019, **45**, 24971–24981.
- 42 S. Fu, R. Yang, J. Ren, J. Liu, L. Zhang, Z. Xu, Y. Kang and P. Xue, *ACS Nano*, 2021, **15**, 11953–11969.
- 43 K. Wang, H. Zhang, A. Shen, P. Zhao, X. Meng, X. Chen, Y. Liu, Y. Liu, T. Gong, W. Wu, X. Fang, P. Wang and W. Bu, *Biomaterials*, 2020, **232**, 119703.
- 44 Y. Guo, X. Zheng, T. Gai, Z. Wei and S. Zhang, *Chem. Commun.*, 2021, **57**, 5754–5757.
- 45 J. C. Yang, Y. Chen, Y. H. Li and X. B. Yin, *ACS Appl. Mater. Interfaces*, 2017, **9**, 22278–22288.
- 46 E. Lin, R. Huang, J. Wu, Z. Kang, K. Ke, N. Qin and D. Bao, *Nano Energy*, 2021, **89**, 106403.
- 47 F. Zhang, G. Lu, X. Wen, F. Li, X. Ji, Q. Li, M. Wu, Q. Cheng, Y. Yu, J. Tang and L. Mei, *J. Controlled Release*, 2020, **326**, 131–139.
- 48 X. Liu, S. Dong, M. Dong, Y. Li, Z. Sun, X. Zhang, Y. Wang, L. Teng and D. Wang, *Int. J. Pharm.*, 2021, **607**, 121034.
- 49 K. Wang, Y. Xiang, W. Pan, H. Wang, N. Li and B. Tang, *Chem. Sci.*, 2020, **11**, 8055–8072.
- 50 Z. Chen, Y. Zeng, N. Chen, M. Zhang, Y. Wang, Z. Pan, J. Yuan, Z. Ye, X. Li, W. Bian, H. Li, K. Zhang, Y. He and X. Liu, *Adv. Healthc. Mater.*, 2022, **11**, e2200044.
- 51 P. Kulkarni, R. G. Balkrishna, D. Ghosh, R. S. Rawat, R. Medwal, B. V. R. Chowdari, Z. Karim and M. V. Reddy, *Mater. Chem. Phys.*, 2021, **257**, 123747.
- 52 S. Bai, N. Yang, X. Wang, F. Gong, Z. Dong, Y. Gong, Z. Liu and L. Cheng, *ACS Nano*, 2020, **14**, 15119–15130.
- 53 Y. Liu, W. Zhen, L. Jin, S. Zhang, G. Sun, T. Zhang, X. Xu, S. Song, Y. Wang, J. Liu and H. Zhang, *ACS Nano*, 2018, **12**, 4886–4893.
- 54 M. Nag, V. Gajbhiye, P. Kesharwani and N. K. Jain, *Colloids Surf., B*, 2016, **148**, 363–370.